

# Daily Land Surface Temperature Reconstruction in Landsat Cross-Track Areas Using Deep Ensemble Learning With Uncertainty Quantification

Shengjie Liu, Siqin Wang, and Lu Zhang

**Abstract**—Many real-world applications rely on land surface temperature (LST) data at high spatiotemporal resolution. In complex urban areas, LST exhibits significant variations, fluctuating dramatically within and across city blocks. Landsat provides high spatial resolution data at 100 meters but is limited by long revisit time, with cloud cover further disrupting data collection. Here, we propose DELAG, a deep ensemble learning method that integrates annual temperature cycles and Gaussian processes, to reconstruct Landsat LST in complex urban areas. Leveraging the cross-track characteristics and dual-satellite operation of Landsat since 2021, we further enhance data availability to 4 scenes every 16 days. We select New York City, London and Hong Kong from three different continents as study areas. Experiments show that DELAG successfully reconstructed LST in the three cities under clear-sky (RMSE = 0.73-0.96 K) and heavily-cloudy (RMSE = 0.84-1.62 K) situations, superior to existing methods. Additionally, DELAG can quantify uncertainty that enhances LST reconstruction reliability. We further tested the reconstructed LST to estimate near-surface air temperature, achieving results (RMSE = 1.48-2.11 K) comparable to those derived from clear-sky LST (RMSE = 1.63-2.02 K). The results demonstrate the successful reconstruction through DELAG and highlight the broader applications of LST reconstruction for estimating accurate air temperature. Our study thus provides a novel and practical method for Landsat LST reconstruction, particularly suited for complex urban areas within Landsat cross-track areas, taking one step toward addressing complex climate events at high spatiotemporal resolution.

**Index Terms**—deep ensemble learning, Landsat, land surface temperature, reconstruction, annual temperature cycle, Gaussian processes, uncertainty quantification

## I. INTRODUCTION

Continuous land surface temperature (LST) data from satellites is fundamental to achieve sustainable development, to understand climate, and to analyze climate impacts on planetary health [1]. Many of the real-world applications rely on satellite LST data, including monitoring wildfires, weather forecasting,

and understanding temperature-related mortality [2], [3], [4]. Although satellites can provide LST data on a large scale, these data are often incomplete due to cloudy weather conditions and sometimes sensor failure [5], [6], [7]. For high spatial resolution satellite data, due to sensor technology, the trade-off between spatial and temporal resolutions further restricts daily data collection. Although daily LST data is crucial for real-world applications, currently we don't have good enough daily LST data at high spatiotemporal resolution [8].

In order to have daily LST data for real-world applications, many efforts have been devoted for LST data reconstruction [9], [10], [11], [12]. These methods are often applied to the MODIS, VIIRS and Himawari-8 LST data that have a spatial resolution of 1-10 km [10], [13]. The annual temperature cycle (ATC) model, for example, is one of the popular methods [14], [15]. The ATC model assumes that daily mean temperature follows a cosine function with three parameters, and the three parameters have their physical meaning, representing the annual mean temperature, the amplitude, and the phase shift that are critical to understand changes over time [16]. However, the ATC model cannot capture daily fluctuation. One direction is to revise the three-parameter ATC model to an enhanced four-parameter ATC model to incorporate reanalysis temperature data [17] or phenology information [14], [18]. Another solution is to use Gaussian processes to model the residuals between the observed and the ATC-reconstructed LST data [19]. These existing methods are often applied to LST data reconstruction at the kilometer resolution due to data availability.

At the kilometer resolution of MODIS and other commonly used LST data, it is impossible to capture temperature heterogeneity within a city [10]. In complex urban areas, temperature changes dramatically over short distances, ranging from a few meters to street blocks [20]. For example, in New York City as shown in Figure 1, many urban parks have been able to reduce daytime temperature with vegetation. The city has complex street blocks exhibiting large temperature variations, but these variations are not captured from the coarse LST data, such as the 4 km resolution gridMET and the 1 km resolution MODIS (Figure 1). The coarse-resolution LST data and the resulting coarse-resolution water masks also make data unavailable in many coastal urban areas with high population density such as Manhattan (Figure 1). Having fine-scale LST data is therefore critical due to the complex landscape, vast temperature heterogeneity, and high population concentration in cities that are more vulnerable to climate

Preprint. S.L. was supported in part by a USC Dana and David Dornsife College of Letters, Arts and Sciences/Graduate School Fellowship. S.L. and L.Z. were supported in part by the National Institute of Environmental Health Sciences of the National Institutes of Health (NIH) under grant number P30ES007048 through the Southern California Environmental Health Sciences Center. The views and conclusions expressed in this study are those of the authors and do not necessarily represent the official policies or endorsements of the NIH. (*Corresponding author: Lu Zhang.*)

S. Liu and S. Wang are with Spatial Sciences Institute, Dornsife College of Letters, Arts and Sciences, University of Southern California, Los Angeles, CA 90089, USA (e-mail: skrisliu@gmail.com; siqinwan@usc.edu).

L. Zhang is with Division of Biostatistics, Department of Population and Public Health Sciences, Keck School of Medicine, University of Southern California, Los Angeles, CA 90089, USA (e-mail: lzhang63@usc.edu).

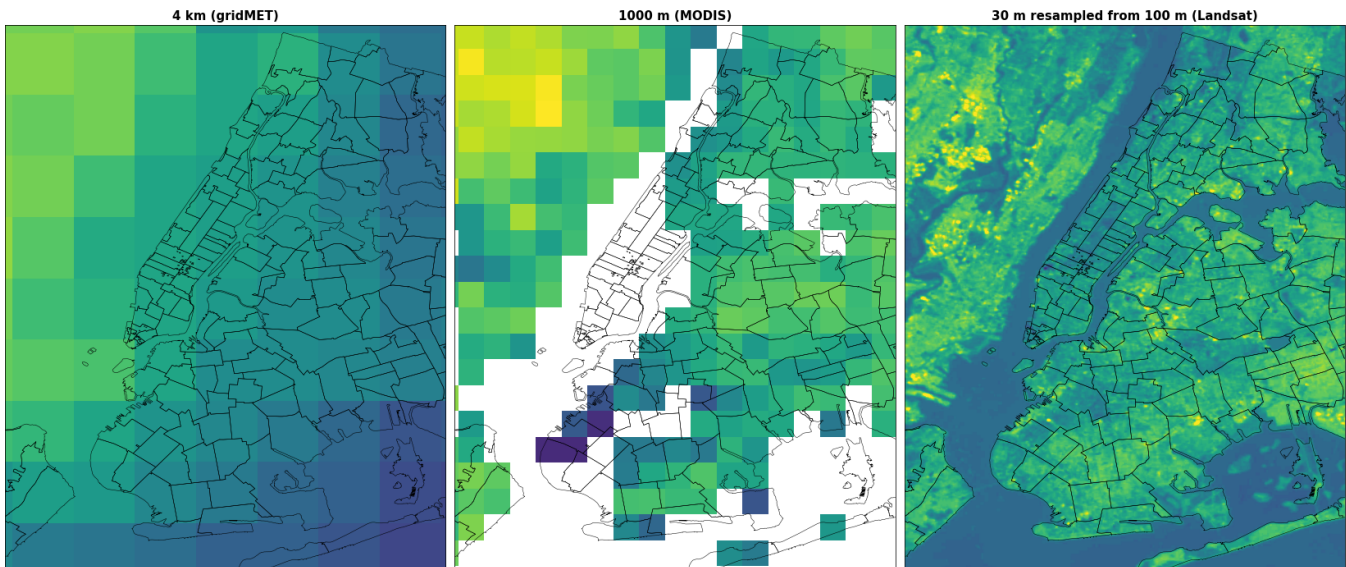


Fig. 1: Spatial resolution comparison of three types of satellite-derived temperature products: gridMET (4 km), MODIS (1 km), Landsat (30 m resampled from 100 m). The overlaid polygons are the New York City merged zip-code boundaries that have daily counts of emergency department visit data. But at the spatial resolution of gridMET (4 km) and MODIS (1 km), these existing LST data are not sufficient to capture temperature variations. Landsat LST can capture temperature variations but is limited by temporal frequency and clouds.

impacts [21]. Additionally, in real-world applications, many datasets are aggregated to small geographical units, such as zip codes (Figure 1). Many socioeconomic and health datasets are available at this level to support research on various topics, including air pollution, respiratory diseases, and temperature-related mortality [22], [23], [24]. However, the development of high resolution temperature data lacks behind, and many real-world applications had to settle to the coarse-resolution LST data [25], [26], [27].

Landsat is the only widely-used satellite series with sufficiently high spatial resolution to capture temperature heterogeneity within a city. Landsat has a revisit time of 16 days, an often-used excuse (in addition to clouds) to eliminate its potential to generate daily LST data. In the existing literature, only a very small subset has explored Landsat LST reconstruction. For example, Zhu et al. (2022) [28] proposed an ATC-based novel method to reconstruct cloudy LST based on a series of procedures including cloud removal, shadow identification, and grouping from spatially adjacent similar pixels. An earlier work used temporal Gaussian processes for daily Landsat LST reconstruction without considering spatial correlation [19]. As a restriction of Landsat’s long revisit time, both studies adopted an inter-annual approach to ensure sufficient data support, making the interpretation of ATC parameters that are supposed to have physical meaning difficult. These methods are also limited to dates with Landsat observations; on many dates without Landsat observations, the uncertainty drawn from these approaches can be large, but the reliability and uncertainty of the reconstruction are unknown.

To generate high resolution LST data on a daily basis, especially in cities, we here propose a framework that consists of two parts: from the perspectives of both data and method.

From the data perspective, we leverage the Landsat cross-track areas and highlight its overlooked role in LST reconstruction. Although Landsat has a revisit time of 16 days, the Landsat cross-track areas (2 observations per 16 days) cover many cities that can benefit from this special setting. For example, the densely-populated New York City is completely situated within two Landsat tracks (Figure 2). Two other cities—London and Hong Kong—in this study also have their majority within the cross-track areas. With both Landsat 8 and 9 satellites in operation since 2021, the frequency is further enhanced to 4 scenes per 16 days, making daily Landsat LST reconstruction for practical applications toward feasible. From the method perspective, in this study, we propose DELAG, a deep ensemble learning method incorporating enhanced ATC models and Gaussian processes for Landsat LST reconstruction. DELAG utilizes deep ensembles to achieve prediction intervals – first of its kind. The enhanced ATC model and Gaussian processes are used to link clear-sky pixels to cloud-covered pixels. There is no LST site within the study areas, and given that many real-world applications require air temperature (instead of LST) derived from satellites [29] and the ability of LST to generate accurate air temperature [30], we validate the proposed method by comparing the air temperature generated from clear-sky LST and reconstructed LST using a simple linear statistical method, a validation approach commonly used in the literature [31], [18].

In the remainder of this paper, we first introduce and visualize the Landsat cross-track areas in Section II. We show that Landsat cross-track areas are sufficiently generalized, in many countries and regions, especially in mid- to high-latitude densely populated areas. We select three representative cities—New York City, London and Hong Kong—across three different

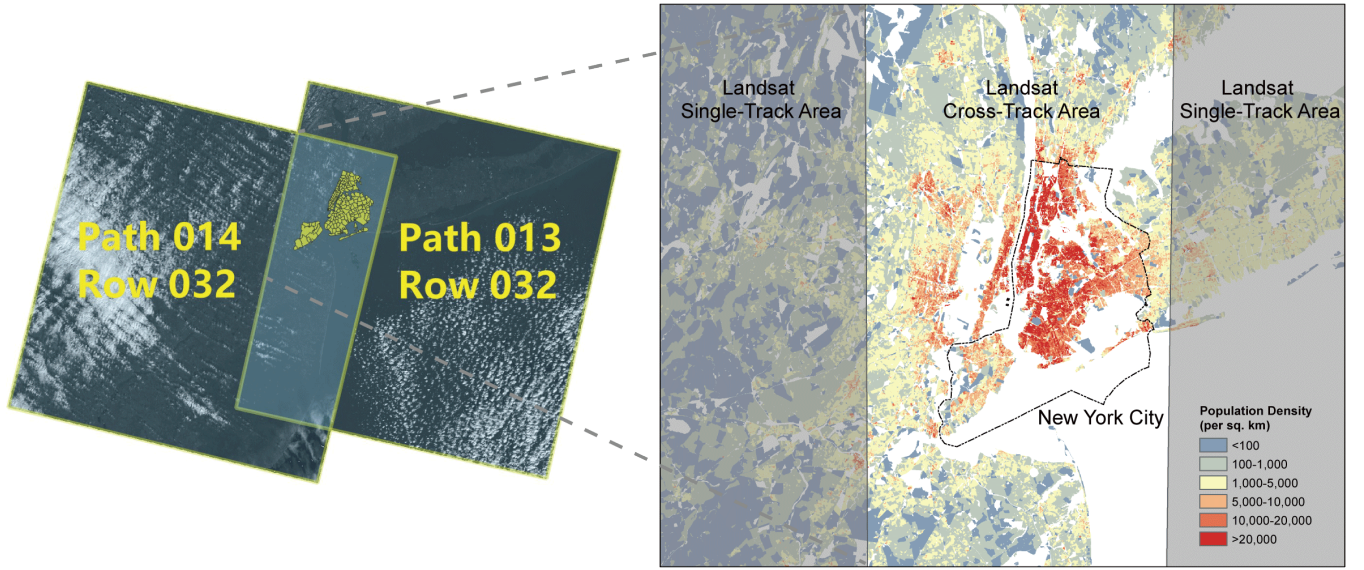


Fig. 2: New York City is situated within the Landsat cross-track areas, completed being covered by two Landsat scenes (Path 014 Row 032, Path 013 and Row 032). This area, New York City and the surroundings, has complex urban landscape and high population density.

continents as study areas here to demonstrate the generalization of the proposed framework. We then detail the proposed method (DELAG), the auxiliary data and validation strategies in Section IV. In Section V, we show the experimental results in the three cities, the ablation analysis, and the indirect validation (and application) with near-surface air temperature data. We discuss the broader impacts and conclude this study in Section VI.

## II. LANDSAT CROSS-TRACK AREAS

The Landsat satellites are a series of polar-orbiting satellites that are designed for land use and land cover monitoring [32]. Since Landsat 4 launched in 1982, the Landsat satellites have thermal sensors onboard that can record land surface temperature. The current operating satellites (Landsat 8 and 9) have two thermal bands at 10.6-11.2  $\mu\text{m}$  (Band 10) and 11.5-12.5  $\mu\text{m}$  (Band 11). As a result of their polar-orbiting nature, each Landsat satellite has a revisit time of 16 days. Between two adjacent Landsat tracks (recording data on two different dates), there is an overlapped area that has dual observations [33]. The cross-track characteristics is often overlooked, as these areas are often assumed insignificant. But in fact, they cover a rather large area, especially at mid- to high-altitude regions, including some densely populated urban areas. Additionally, from a data perspective, we have the potential to recover the entire LST surface on Earth from the partial observations.

In the following calculation and visualization, we demonstrate that the Landsat cross-track areas are not as insignificant as previously assumed. In the current specification, Landsat captures each scene in a dimension of 185 km  $\times$  180 km following its polar-orbiting trajectory [32]. In Figure 2, we show two sample scenes and highlight the cross-track areas that completely cover New York City. Landsat scenes have a width of 185 km ( $L_{\text{landsat}}$ ) in a roughly horizontal direction,

with a  $8.2^\circ$  shift parallel to latitude, leading to a horizontal coverage of 183.1 km. Every 16 days, a Landsat satellite travels 233 tracks, and then revisits. The ratio  $\phi_{\text{lat}}$  between the horizontal length of all Landsat scenes within a revisit period (16 days, 233 tracks) and the latitude (with a length of  $L_{\text{lat}}$ ) can be calculated as

$$\phi_{\text{lat}} = \frac{L_{\text{landsat}} \times \cos(8.2^\circ)}{L_{\text{lat}}} \times 233. \quad (1)$$

The ratio reaches its minimum (1.07) at the Equator, meaning that about 7% of the areas at the Equator are covered by two Landsat scenes per 16 days. The percentage of overlapping areas increases with latitude increasing and reaches to a ratio of 1.50 at  $45^\circ$  latitude: half of the areas at  $45^\circ\text{N}$  and  $45^\circ\text{S}$  are covered by two Landsat scenes per 16 days. We compute and visualize these Landsat cross-track areas in Figure 3, and the percentage of the cross-track areas in each country and region in Figure 4. Eleven countries and regions are 100% located in the Landsat cross-track areas, and many countries and regions have half of their areas located in the Landsat cross-track areas. Mid-to-high-latitude countries and regions, including most in Europe, Canada, and Russia have a high percentage of cross-track areas. At the metropolitan level, the cross-track areas cover many densely-populated urban areas including New York City (100%), London (>95% areas), and Hong Kong (>90% urban areas). As a combined result of cross tracks and dual satellites, we have four scenes per 16 days in these cities, making it toward feasible for daily Landsat LST reconstruction. In this study, we select New York City, London and Hong Kong as the three representative cities as study areas to demonstrate the generalization of the proposed framework and the proposed method.



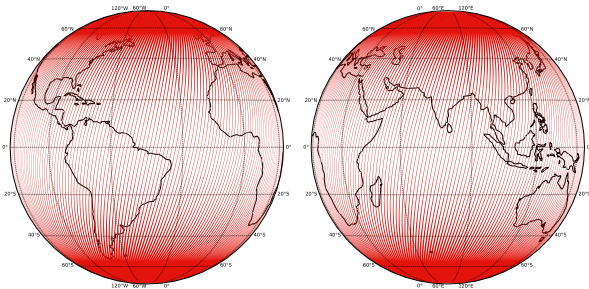


Fig. 3: Global areas covered by two or more Landsat scenes within a revisit period of 16 days, marked in red.

### III. STUDY AREAS AND DATA

#### A. Study Areas

1) *New York City*: New York City (NYC) is a megacity with the highest population density in the United States and is the primary case in this study for three reasons. First, the city’s health department releases daily syndromic surveillance data (e.g., respiratory emergency department visit) at the zip code level to the public. This dataset has been commonly used in real-world applications to investigate how various air pollutants and other environmental exposures affect human health [24], [34], [35]. However, currently, there is no daily LST data available that is able to distinguish temperature exposures at each zip code, making it impossible to address the impacts and disparities of temperature exposure within the city. Second, NYC is completely situated within the Landsat cross-track areas (Figure 2), making it an ideal study case for the proposed framework. Third, NYC has complex urban landscape and high temperature variations. With 8.3 million residents, the city has a population density of 11,000 per  $\text{km}^2$ , about 110 residents per Landsat thermal pixel ( $100 \text{ m} \times 100 \text{ m}$ ). Given the complex urban setting, LST varies from locations to locations. High spatiotemporal resolution LST data are therefore necessary.

2) *London*: To demonstrate the generalization of the proposed framework, London is selected as the second study case. London is the largest city in the U.K. and Western Europe, with 8.8 million residents in  $1,572 \text{ km}^2$  area (5,690 per  $\text{km}^2$ ). Apart from a small portion in the southeast, the majority of London falls within the Landsat cross-track areas (Path 202 Row 024, Path 201 Row 024). London has two levels of small geographical units (with 983 Middle Super Output Areas and 4,835 Lower Super Output Areas) that are finer than  $1 \text{ km}^2$  – the MODIS resolution (Figure 5). These geographical units have mortality and other socioeconomic and health statistics that can be used for social good, but as a result of the lack of high resolution temperature data, existing studies had to settle on using coarse resolution temperature data that limits their capability [22], [36], [37].

3) *Hong Kong*: Hong Kong is selected as the third study area to demonstrate the generalization of the proposed framework and method across different continents and climate zones. Hong Kong is a coastal city in Asia, with a land area of  $1,073 \text{ km}^2$ , housing 7.5 million population (6,989 per  $\text{km}^2$ ). Similar to New York City and London, most urban areas are

also situated within the Landsat cross-track areas (Figure 5). The city maintains a large portion (75%) of undeveloped lands, further intensifying population density. As a high-density and subtropical city, Hong Kong faces various extreme climate events, in need of high spatial resolution temperature data.

#### B. Data and Preprocessing

1) *Landsat Land Surface Temperature*: We obtained all 2023 Landsat 8 and 9 Collection 2 Level-2 science products and used the analysis-ready LST data from the thermal band (Band 10). NYC is completely located within two Landsat scenes (Path 013 Row 032, and Path 014 Row 032, Figure 2), with a total number of 92 scenes. London is completely covered by one scene (Path 201 Row 024), and has its majority covered by another (Path 202 Row 024), with a total number of 86 scenes. Hong Kong has most of its urban areas covered by two scenes (Path 121 Row 045, Path 122 Row 044), with a total number of 91 scenes.

Before conducting the experiments, we went through a series of preprocessing, mainly on cloud masking and removal. We first checked the cloud band from the Level-2 products and masked out all data labeled as unclear. The cloud masks are generated from the Fmask algorithm and are not 100% perfect as noted from data description. We then double-checked visually with the imagery and cloud masks using a  $3 \times 3$  split. Within each split, if the pixels were mostly flagged as clear but were in fact covered by clouds, we masked out all the pixels within the split. In some cases, within each split, all pixels within the split appeared clear and most pixels were flagged as clear, but some pixels were flagged as not clear (mostly at coastline), we flagged this split as clear. After preprocessing, we have three types of data: dates under clear-sky situations, dates under partially-cloudy situations, and dates without valid observations (100% cloudy or no Landsat overpass).

2) *ERA5 Reanalysis LST Data*: The proposed method DELAG includes an enhanced 4-parameter ATC model that has the capability to capture daily temperature fluctuation. The additional variable in the enhanced ATC model needs to be a continuous temperature record, and we used the skin temperature from ERA5 daily aggregated data [38]. The ERA5 reanalysis products have a resolution of 11 km. Each pixel is matched to the nearest ERA5 LST value.

3) *Annual Mean Spectral Reflectance*: In order to link valid-observed pixels to cloud-covered pixels, the proposed method DELAG uses Gaussian processes to model the residuals between observed LST and ATC-reconstructed LST. The residuals are related to ground objects, which can be distinguished through spectral reflectance. We obtained the mean surface reflectance from 2022-2024 for four spectral bands (red, green, blue, and near infrared) from the Sentinel-2 products. The data is then resampled and matched with the Landsat ones. We obtained through Sentinel-2 instead of Landsat because Sentinel-2 has a higher revisit frequency, but the influence should be negligible. We also added the  $x$  and  $y$  coordinates, along with the spectral bands, as the features used in Gaussian processes.



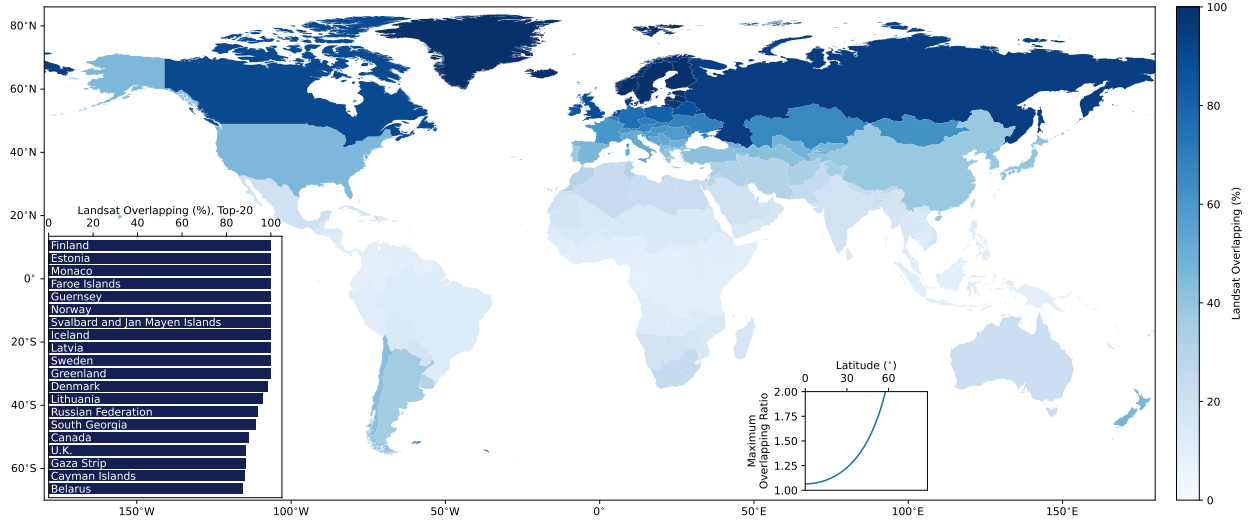


Fig. 4: Percentage of Landsat cross-track areas in global countries and regions. The top-20 are listed on the lower left. The ratio of Landsat coverage as a function of latitude is shown in the middle right.

4) *Near-surface Air Temperature Data*: There is no in-situ LST site within the three cities, thus a direct comparison with in-situ LST in our study areas is not possible. However, given that most real-world applications require near-surface air temperature instead of LST, and many seamless LST data will be used for generating near-surface air temperature, we can indirectly validate the reconstruction with near-surface air temperature data (details in method Section IV-B3). This is an approach commonly used in the existing literature [18], [31]. For this purpose, we obtained air temperature data from meteorological stations. For New York City, we obtained data from 7 stations from the Automated Surface/Weather Observing Systems (ASOS/AWOS) maintained by the National Weather Service. For London, there are 6 meteorological stations. These data were obtained through Meteostat, an open source Python library that archives meteorological data from public sources. For Hong Kong, we obtained air temperature data from 23 stations from the Hong Kong Observatory. The locations of the meteorological stations in the three cities can be found in Figure 5.

## IV. METHODOLOGY

### A. DELAG: Deep Ensemble Learning With Annual Temperature Cycles and Gaussian Processes

The proposed method DELAG is a two-stage model, including enhanced annual temperature cycles (ATC) and Gaussian processes (GP). In the first stage, for each pixel, DELAG reconstructs LST using valid-observed data through an enhanced ATC model. The model solution is solved using deep ensemble learning by minimizing the loss function via Adam optimization. A total of 200 model snapshots are obtained to generate ensemble predictions and quantify uncertainty. In the second stage, the residuals between ATC-reconstructed LST and the valid-observed Landsat LST from the non cloud-covered pixels are calculated. Within each day, the residuals are related to certain surface properties, which can be used as

features to predict the residuals. The residuals, as a surface of random processes, can be modeled through Gaussian processes based on valid-observed pixels. Within the same day, this surface can be generalized to cloud-covered pixels, thus also achieving LST reconstruction for cover-covered pixels on dates with valid-observed LST. The uncertainty on dates with valid-observed LST is then quantified from both models from the first stage (ATC) and second stage (GP). For dates without any valid-observed LST (100% cloud cover or no Landsat overpass), only the first part of the estimations will be applied.

Overall the proposed method DELAG can be expressed as

$$\mathcal{T}_s^R(d) = \mathcal{T}_s^{ATC}(d) + \mathcal{T}_s^{GP}(d), \quad (2)$$

where  $d$  is day of year,  $s = [x, y]$  is individual pixel's indexes,  $\mathcal{T}_s^{ATC}(d)$  is the ATC-reconstructed temperature as a function of day of year of pixel  $s$ , and  $\mathcal{T}_s^{GP}(d)$  is the temperature residual estimated from GP.

On day of year  $d$ , given the coarse-resolution ERA5 reanalysis LST value  $\mathcal{T}^c(d)$ , a set of valid-observed Landsat pixels  $\mathbf{s}_d$ , and the corresponding valid-observed LST data  $\mathcal{T}(d, \mathbf{s}_d)$ , Equation 2 can be written out as

$$\mathcal{T}_s^R(d) = C_s + A_s \cos(2\pi/365(d - \phi_s)) + b_s \mathcal{T}^c(d) + \mathcal{GP}_d(s, \mathbf{s}_d), \quad (3)$$

where  $C_s + A_s \cos(2\pi/365(d - \phi_s))$  is the classic ATC model with  $\{C_s, A_s, \phi_s\}$  as three location-dependent ATC parameters,  $b_s$  is a location-specific parameter to capture daily fluctuation (making it an enhanced ATC). And  $\mathcal{GP}_d(s, \mathbf{s}_d)$  is to use a daily-specific GP model  $\mathcal{GP}_d(\cdot)$  to account for the temperature residuals between valid-observed Landsat LST data and ATC-reconstructed LST by modeling the relationship between certain surface properties and the valid-observed LST residuals  $\mathcal{T}(d, \mathbf{s}_d) = \{\mathcal{T}_{k,d}\}_{k \in \mathbf{s}_d}$  from a set of valid-observed pixels  $\mathbf{s}_d$ .

1) *Enhanced Annual Temperature Cycles*: We use the PyTorch deep learning framework to find the solutions of the

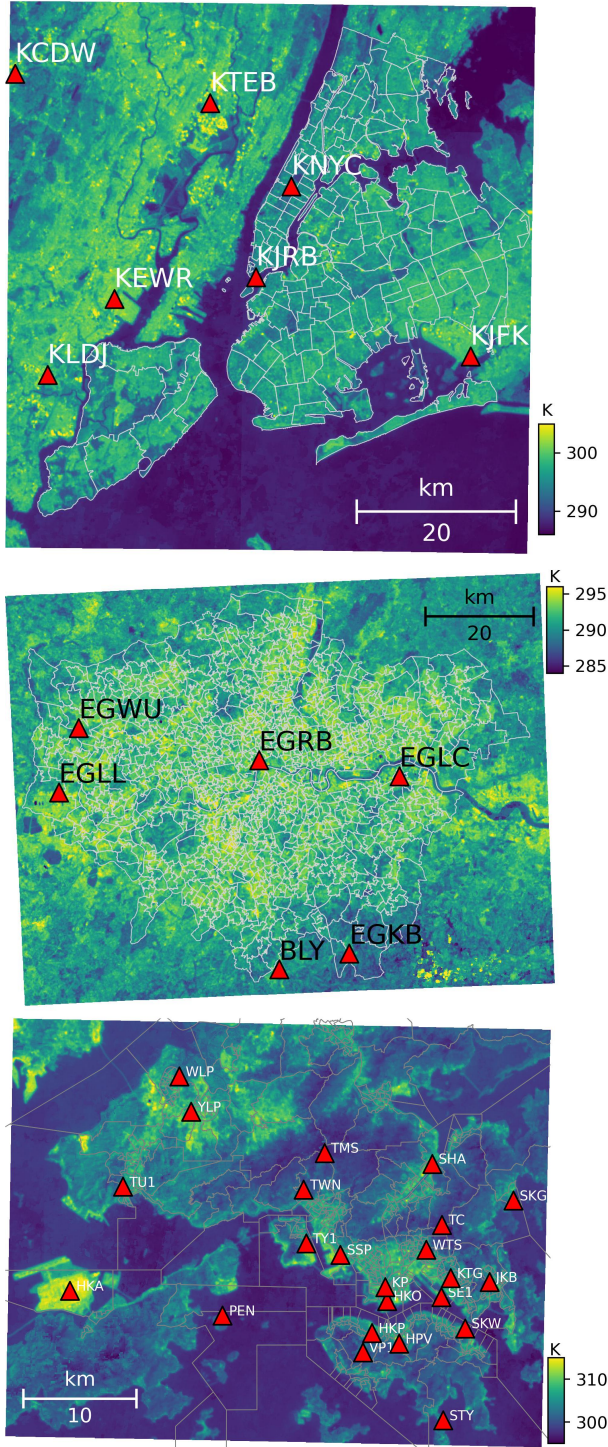


Fig. 5: Meteorological stations of the three cities, overlapped with annual mean temperature and geographical unit boundaries (NYC: 135 merged zip codes, London: 983 Middle Super Output Area, Hong Kong: 452 District Council Ordinary Election Constituency Boundaries). New York City: 7 stations. London: 6 stations. Hong Kong: 23 stations.

model. In the first stage (eATC), we minimize the L1 loss between the observed LST  $\mathcal{T}$  and the eATC-reconstructed LST  $\hat{\mathcal{T}}^{ATC}$ . This process is equivalent to maximizing a Laplace

likelihood, and can be written out as (with the location index  $s$  omitted)

$$p(\mathcal{T} | \omega) \propto \exp\left(\frac{-|\mathcal{T} - \hat{\mathcal{T}}^{ATC}|}{\beta}\right), \quad (4)$$

where  $\omega = \{C, A, \phi, b\}$  is the parameters of eATC that is used to calculate  $\hat{\mathcal{T}}^{ATC}$ , and  $\beta$  is a scale factor of the Laplace distribution.

2) *Gaussian Processes to Model LST Residuals*: On the same date, LST residuals ( $\mathcal{T}^\epsilon = \mathcal{T} - \mathcal{T}^{ATC}$ ) are related to certain surface property. We can then model this surface from GP by linking certain features and LST residuals from the valid-observed pixels. This GP model can be used to predict the LST residuals to the cloud-covered pixels, as we assume the LST residuals follow the same random processes related to surface property within the same day. For features, we use the annual mean spectral reflectance from red, green, blue, and near infrared bands from Sentinel-2, and add the two coordinate variables to capture some spatial trends. The GP model is built with GPyTorch, a GP framework built on PyTorch for scalable Gaussian processes through variational and Blackbox Matrix-Matrix inference [39].

On day of year  $d$ , we assume the LST residuals  $\mathcal{T}^\epsilon$  follow a GP with mean function  $m(s)$  and covariance function  $k(\cdot, \cdot)$  (with  $d$  omitted):

$$\mathcal{T}^\epsilon(s) \sim \mathcal{GP}(m(s), k(\cdot, \cdot)), \quad (5)$$

where  $k(s, s')$  defines the covariance between two pixels  $(s, s')$  over LST residuals  $\mathcal{T}^\epsilon(s)$  and  $\mathcal{T}^\epsilon(s')$  based on their similarity.

Given known LST residuals  $\mathcal{T}^\epsilon(s_d)$  from valid-observed Landsat LST pixels  $s_d$ , we have their feature representation (spectral bands)  $\mathbf{X}_{s_d}$  and a covariance matrix  $\mathbf{K}_{s_d}$  that records the covariance between all valid-observed Landsat LST (training data points). We train the model by maximizing the log-likelihood function, which can be written as (with  $s_d$  omitted):

$$\begin{aligned} \log p(\mathcal{T}^\epsilon | \mathbf{X}, \mathbf{K}, \Theta) &= -\frac{1}{2} (\mathcal{T}^\epsilon - m(\mathbf{X}))^\top \mathbf{K}^{-1} (\mathcal{T}^\epsilon - m(\mathbf{X})) \\ &\quad - \frac{1}{2} \log |\mathbf{K}| - \frac{n}{2} \log(2\pi), \end{aligned} \quad (6)$$

where  $\Theta$  is the hyperparameters within the covariance function; in our experiments, we used the radial basis function (RBF) kernel.

3) *LST Residuals for Cloud-Covered Pixels*: Once the GP model is built, we can estimate the LST residuals over cloud-cover pixels. On day of year  $d$ , given non-cloud-covered pixels  $s_d$  and cloud-cover pixels  $s_d^*$ , their feature representations  $\mathbf{x}_s$  and  $\mathbf{x}_{s^*}$ , the mean of the LST residuals modeled by GP ( $\mathcal{T}_{s^*}^{GP}$ ) for the cloud-cover pixels is:

$$\mathcal{T}_{s^*}^{GP} = \mu(\mathbf{x}_{s^*}) = \mathbf{k}_{s^*}^\top (\mathbf{K} + \sigma^2 \mathbf{I})^{-1} \mathcal{T}_s^\epsilon, \quad (7)$$

where  $\mathbf{k}_{s^*} = [k(\mathbf{x}_i, \mathbf{x}_{s^*})]_{i=1}^n$  is the covariance vector between training points and  $\mathbf{x}_{s^*}$ ,  $\mathbf{K}$  is the  $n \times n$  covariance matrix

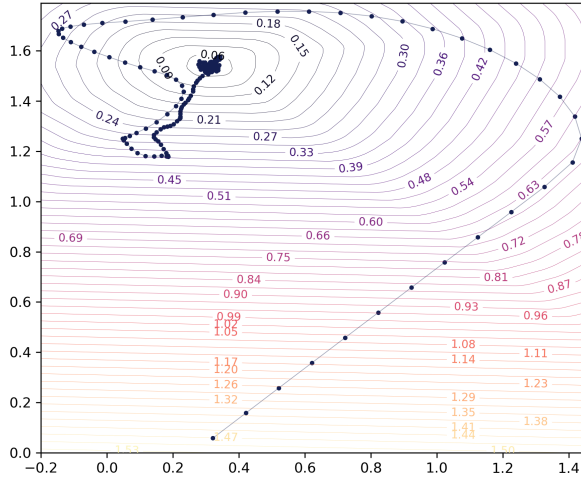


Fig. 6: Demo showing the loss surface and the model’s trajectory in training. As training progresses, the loss value becomes sufficiently small, with 334 out of 425 snapshots falling below the smallest contour level of 0.06. With slight variations in these solutions, leveraging all snapshots as an ensemble allows the proposed DELAG method to deliver robust predictions and provide uncertainty quantification.

of the training points,  $\sigma^2$  is the observed noise. The prediction variance, which is used for uncertainty quantification, is calculated as

$$\sigma^2(\mathbf{x}_{s^*}) = k(\mathbf{x}_{s^*}, \mathbf{x}_{s^*}) - \mathbf{k}_{s^*}^\top (\mathbf{K} + \sigma^2 \mathbf{I})^{-1} \mathbf{k}_{s^*}. \quad (8)$$

The calculation is accelerated through GPyTorch.

4) *Deep Ensemble Learning to Find Model Solutions and Achieve Uncertainty Quantification*: Given the complexity of the model as a non-convex function, it is very difficult, if not impossible, to find the global optimized set of parameters. In the PyTorch deep learning framework, we use the Adam optimizer (a variant of stochastic gradient descent) [40] to minimize the L1 loss to find the optimized solutions in the first step. In training the model, the training loss will eventually flatten and fluctuate, but cannot reach a global minimum. In Figure 6, near the end of training, 334 out of 425 snapshots all fall below the smallest contour level (loss < 0.06). At this phase of the training, all snapshots are acceptable optimized solutions of the model. With each iteration, the parameters update again, resulting another snapshot of model parameters. The disagreement drawn from these snapshots of parameters is large enough, and utilizing the disagreements among these snapshot solutions has become a popular method to achieve ensemble learning or quantify uncertainty in deep learning [41], [42], [43]. Ensemble learning to achieve more robust and reliable prediction is also common in weather predictions and remote sensing [44], [45].

We take advantage of these snapshot solutions to generate ensemble predictions, revising Equation 4 to include an index  $j$  for these optimized solutions:

$$p(\mathcal{T} | \omega) = \frac{1}{J} \sum_j p(\mathcal{T} | \omega_j). \quad (9)$$

This ensemble process can be seen as the posterior predictive distribution over a uniform prior.

5) *Uncertainty Quantification*: The variance of Landsat LST comes from the cross-day variance (modeled via enhanced ATC) and within-day variance (modeled via GP). Using the law of total variance, we decompose the total variance of  $\mathcal{T}$  into two components:

$$\text{Var}(\mathcal{T}) = \mathbb{E}[\text{Var}(\mathcal{T} | D)] + \text{Var}(\mathbb{E}[\mathcal{T} | D]), \quad (10)$$

where  $\mathbb{E}[\text{Var}(\mathcal{T} | D)]$  is the within-day variance and  $\text{Var}(\mathbb{E}[\mathcal{T} | D])$  is the cross-day variance. Therefore, we can simply add the quantified uncertainty together to achieve the final uncertainty quantification:

$$\text{Var}(\mathcal{T}) = \text{Var}(\mathcal{T}^{ATC}) + \text{Var}(\mathcal{T}^{GP}). \quad (11)$$

In DELAG, we obtain 200 snapshots (200 predictions) from the enhanced ATC models. We can then easily obtain the 95% confidence intervals (CI) from the 200 snapshots. GP models inherently generate uncertainty quantification and prediction intervals. We then add the upper and lower predictions from the two stages to estimate the 95% CI. The uncertainty quantification applies to dates with clear-sky situations and dates with partially-cloudy situations. For dates without any valid-observed LST, the uncertainty quantification reduces to enhanced ATC only.

## B. Validation Strategies

Considering the four different situations (clear sky, partially cloudy, no valid Landsat pixels due to 100% cloud cover, and no valid Landsat pixels due to no Landsat overpass), we design three different validation strategies.

1) *Validation With Landsat Clear-Sky Observations Under Real-World Cloud Patterns*: We first validate the result using clear-sky observations under real-world cloud patterns. We randomly select a few dates that have most clear pixels and then mask out some pixels as test data (under some hypothetical cloud pattern). These hypothetical masks are randomly selected from some real-world cloud patterns observed from other dates. This validation strategy can validate results under clear-sky situations.

2) *Validation With Partially-Cloudy Data*: For dates with partially-cloudy situations, the percentage of clouds has a significant impact on the solar energy balance. Under partially-cloudy situations, the valid-observed LST pixels should not be considered as clear-sky pixels. If the percentage of clouds is high enough, the valid-observed LST pixels are close to the overcast situations, as the valid-observed pixels are blocked by clouds and non-observable most of the time (depending on percentage of clouds). Therefore, we separately validate the results under partially-cloudy situations, focusing on dates with more than 80% cloud covers. For this setting, we hold out 20% of the valid-observed pixels and use them as test data.

3) *Validation Via Estimating Near-Surface Air Temperature*: Since there is no in-situ LST site in the three cities, a direct comparison with in-situ LST data is not possible. However, because there is a strong correlation between LST and near-surface air temperature, especially under cloudy



conditions [46], we can indirectly validate the results with in-situ air temperature data, an approach commonly used in the existing literature [31], [18]. More importantly, the capability to generate accurate near-surface air temperature data is critical for many applications, especially for those related to health sciences [47]. If the reconstructed LST can achieve comparable results in estimating near-surface air temperature compared with the valid-observed LST, the reconstruction is considered successful. For this purpose, similar to previous studies, we adopt a simple statistical approach developed by Janatian et al. (2017) [48] to generate near-surface air temperature based on LST:

$$\mathcal{T}_a = \mathcal{T}_{lst} \times \alpha_1 + V_{ndvi} \times \alpha_2 + V_{elv} \times \alpha_3 + V_{sol} \times \alpha_4 + V_{sza} \times \alpha_5 + c, \quad (12)$$

This is a linear equation that consists of five variables. Apart from LST, the equation includes NDVI ( $V_{ndvi}$ ), elevation ( $V_{elv}$ ) and solar radiation factor ( $V_{sol}$ ) to account for local conditions, and solar zenith angle ( $V_{sza}$ ) to account for seasonal changes. We apply this equation once for all meteorological stations within a city, but separately for the valid-observed LST and the reconstructed LST. The LST reconstruction results are considered good when the generation of air temperature from reconstructed LST has similar performance from the clear-sky LST.

4) *Evaluation Metrics*: We use four standard metrics for validation: mean absolute error (MAE), root mean square error (RMSE), coefficient of determination ( $R^2$ ), and bias (Bias).

### C. Training Setup

The experiments were conducted on Python using the PyTorch framework [49]. For ATC fitting, we used the Adam optimizer with a learning rate of 0.1 for 1200 epochs. The 200 ensemble predictions were obtained through every 4 epochs in the final 800 epochs. For Gaussian processes, we used GPyTorch [39], a popular GP framework built upon PyTorch. We used a mini batch of 1024 and the variational inference with 512 inducing points for fast GP computation. The training was conducted with the Adam optimizer with a learning rate of 0.05 for 50 epochs and then of 0.005 for 10 epochs.

## V. RESULTS AND ANALYSIS

### A. Experimental Setup

We conducted three sets of experiments to exam the performance of the proposed method under different cloud conditions. In the first set of experiments, we subset a part of the core urban areas for testing, identified a few dates with 0% cloud cover, and randomly selected real-world cloud patterns from a different date as the hypothetical clouds. This set of experiments is to test the proposed method in reconstructing LST under data-rich, clear-sky situations. Test data are from clear-sky LST pixels that are masked out with some real-world cloud pattern from other dates during training. The second set of experiments was conducted over all data, with this validation strategy specifically targeting heavily cloudy situations (>80%). On these dates, the valid-observed LST is not clear-sky LST but rather similar to overcast situations

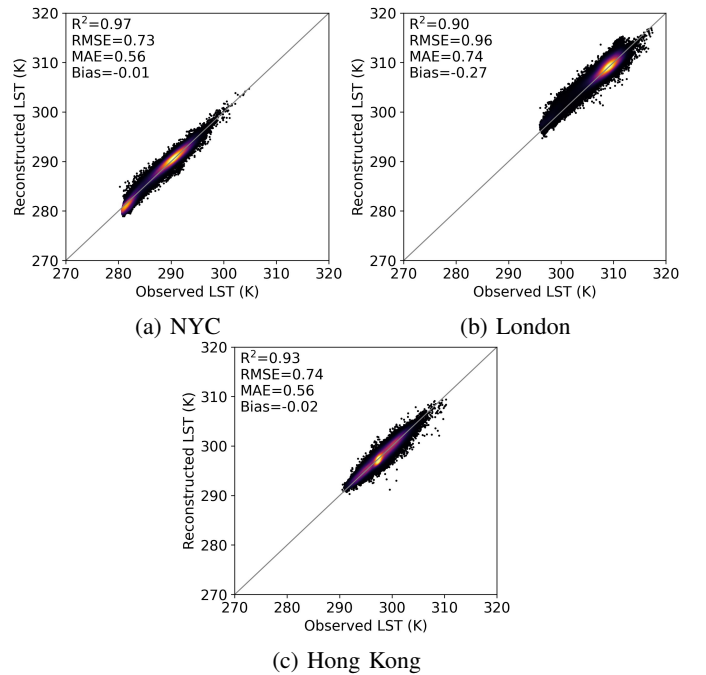


Fig. 7: Scatter plot between reconstructed LST and observed LST under clear-sky situations with real-world cloud patterns. The corresponding reconstruction is shown in Figure 8.

because of the high percentage of clouds (the satellite was only able to record data because there were a few gaps between the clouds). Test data are from 20% of the valid-observed LST under the heavily-cloudy situations that were held out during training. This set of experiments is to test the proposed method in partially-cloudy and heavily-cloudy situations. In the third set of experiments, as there is no in-situ LST site within the three cities, we are not able to test the proposed method under completely overcast (100%) or without Landsat overpass situations. Alternatively, we adopted a common approach in the literature [31], [18] and validate the reconstruction results indirectly by comparing its capability to estimate near-surface air temperature data (detailed earlier in section IV-B3). This set of experiments can test LST reconstruction under all situations, but we focus on cloudy situations or without Landsat overpass. These above-mentioned three validation strategies are detailed in the section IV-B.

### B. Results Under Clear-Sky Situations With Real-World Cloud Patterns

We first show the results under clear-sky situations. We show the scatter plots between the observed and reconstructed LST in Figure 7, along with the corresponding cloud patterns, reconstructed LST and residuals in Figure 8. The proposed method successfully achieved LST reconstruction reconstructed under clear-sky situations with real-world cloud patterns from other dates. Under 52.0% cloud coverage, the proposed method reached a reconstruction result of  $R^2=0.97$ ,  $RMSE=0.73$  K,  $MAE=0.56$  K, and  $Bias=-0.01$  K for NYC (prediction date: 2023-04-01, cloud pattern date: 2023-06-04). Under 52.03% hypothetical cloud cover, the proposed method

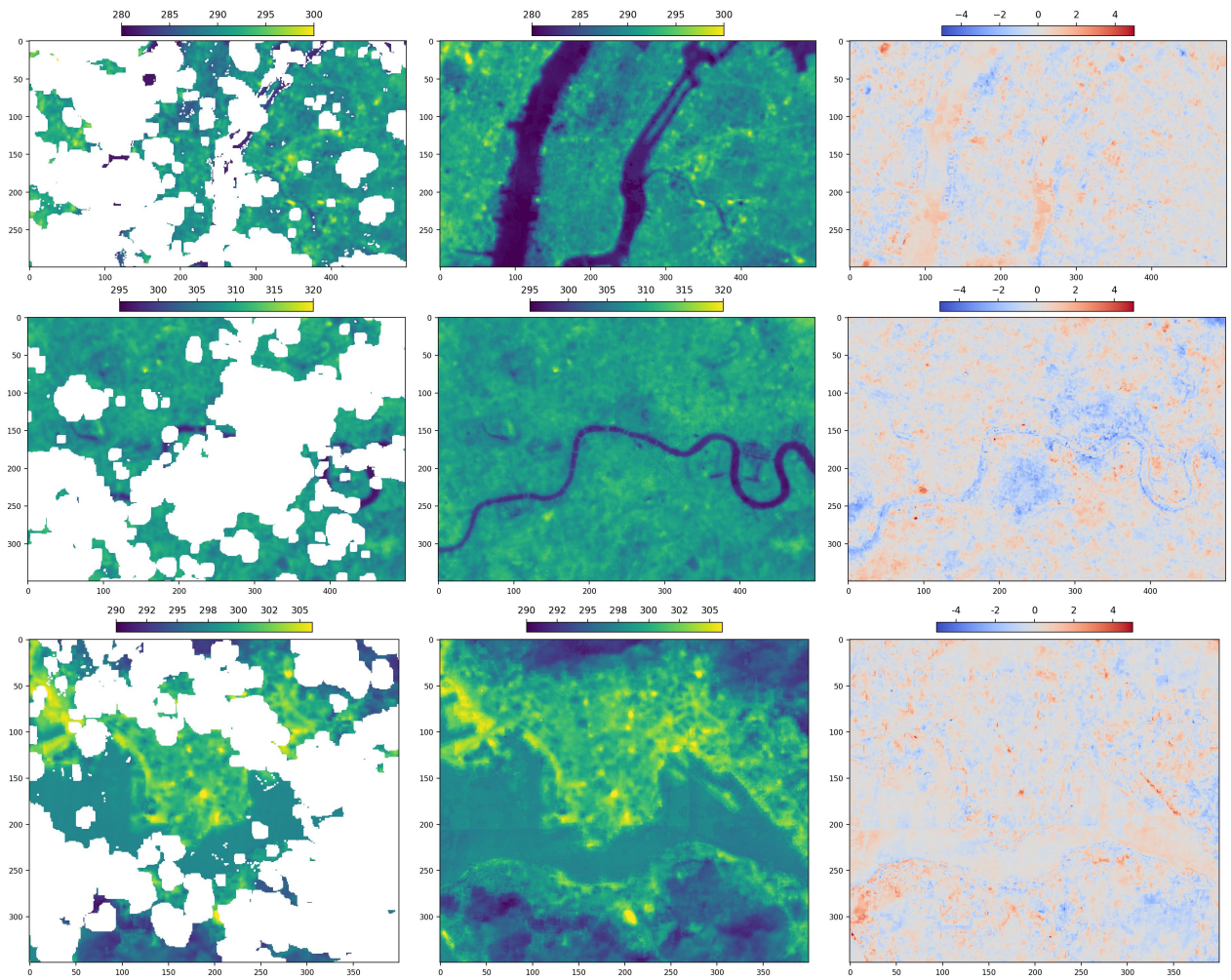


Fig. 8: Results under clear-sky situations with real-world cloud patterns. From left to right: LST with real-world cloud patterns, reconstruction, residuals between observed LST and reconstructed LST. From top to bottom: NYC ( $R^2=0.97$ ,  $RMSE=0.73$  K,  $MAE=0.56$  K,  $Bias=0.01$  K); London ( $R^2=0.90$ ,  $RMSE=0.96$  K,  $MAE=0.74$  K,  $Bias=0.27$  K); Hong Kong ( $R^2=0.93$ ,  $RMSE=0.74$  K,  $MAE=0.56$  K,  $Bias=0.02$  K). The corresponding scatter plots are shown in Figure 7.

reached a reconstruction result of  $R^2=0.90$ ,  $RMSE=0.96$  K,  $MAE=0.74$  K, and  $Bias=-0.27$  K for London (prediction date: 2023-09-06, cloud pattern date: 2023-06-18). Under 56.2% cloud coverage, the proposed method reached a reconstruction result of  $R^2=0.93$ ,  $RMSE=0.74$  K,  $MAE=0.56$  K, and  $Bias=-0.02$  K for Hong Kong (prediction date: 2023-11-17, cloud pattern date: 2023-06-26). All these reconstructions are within the sensor’s accuracy [7]. From the reconstruction images and the residuals (Figure 8), we can see that the reconstruction aligns near perfectly with the observed data.

### C. Results Under Heavily-Cloudy Situations

In the second set of experiments, we mainly tested the proposed method under heavily-cloudy situations. In heavily-cloudy situations or even partially-cloudy situations, the valid-observed LST values not covered by clouds should not be considered as clear-sky LST, because the majority of solar energy is reflected back by the heavy clouds compared to the clear-sky situations. The received solar energy is different from a clear-sky condition and depends on the cloud conditions

(e.g., percentage of cloud covers, thickness, opacity) [50]. These valid-observed LST pixels are only observable due to no direct clouds on top of them, but in the next hours they are likely to be blocked when clouds shift a few hundred meters away. Therefore, these heavily-cloudy and even partially-cloudy situations should be treated differently from the clear-sky situations (especially when the percentage of clouds is over 80%) and should be tested separately. For this purpose, we designed this set of experiments. We selected a few dates that have more than 80% cloud covers (2023-04-18 for NYC, 2023-05-16 for London, 2023-05-25 for Hong Kong), and used only 80% of the available valid-observed pixels for training. The remaining 20% were reserved for testing.

The results are shown in Figure 9. Quantitatively, the proposed method achieved LST reconstruction results of  $R^2=0.85-0.98$ ,  $RMSE=0.84-1.62$  K,  $MAE=0.62-1.23$  K, and  $Bias=-0.67-0.21$  K for the three cities. These reconstructions were obtained with cloud coverage of 83.6%-85.6%. Compared to clear-sky situations, the reconstructed LST images under heavily-cloudy situations clearly have some patterns showing



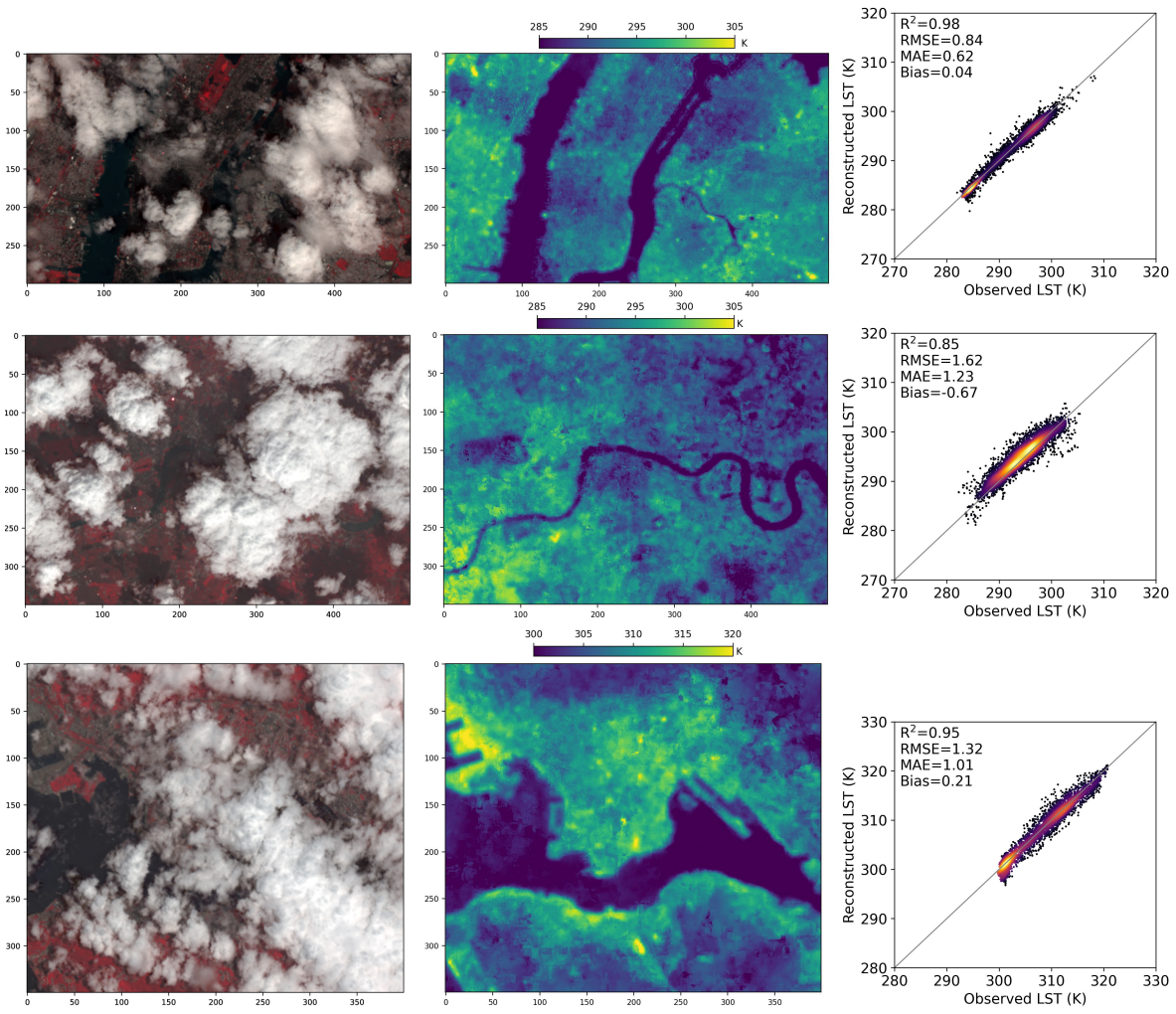


Fig. 9: Results under heavily-cloudy situations. From left to right: valid-observed LST, reconstructed LST, scatter plot between reconstructed LST and the 20% observed LST reserved for testing. From top to bottom: NYC, London, Hong Kong.

the effects of heavy cloud coverage on LST. For example, for the NYC case (Figure 9), the central north areas appear to have relatively lower LST values under heavily-cloudy situations than it is supposed to be under clear-sky situations; and as shown from the image (Figure 9), these areas are most affected by clouds. Similarly, the eastern part of London (Figure 9) and the central part of Hong Kong also shows relatively lower LST values compared to clear-sky situations. These quantitative results and qualitative visualizations demonstrate the success of the proposed method for LST reconstruction under heavily-cloudy situations.

#### D. Indirect Validation via Estimating Near-Surface Air Temperature

To further validate the proposed method, we tested the performance of the reconstructed LST in estimating near-surface air temperature. To compare the performance of estimating near-surface air temperature through valid-observed LST (under clear-sky situations) and reconstructed LST (under cloud-covered and no Landsat overpass situations), ideally we can apply them together to build one simple linear model, and

the results should be consistent regardless of LST situations. But given that there are more cloud-covered and no Landsat overpass data points, the linear model could be dominated by these data points and thus biased. For validation purposes, we should fit two linear models separately, one for clear-sky valid-observed LST situations, and another for cloud-covered or no Landsat overpass situations. The reconstruction is good if the performance of the latter model has similar capability of the former model. Thus, we built two models using all stations from one city, separately for the two LST situations. We plot the estimated air temperature and in-situ air temperature for each station in Figure 10 for New York City, in Figure 11 for London, and in Figure 12 for Hong Kong. The results, overall and on individual stations, are shown in Tables I, II, II, respectively. Overall, the proposed method achieved similar results on using reconstructed LST to estimate near-surface air temperature ( $R^2=0.93$ ,  $RMSE=2.11$  K,  $MAE=1.72$  K), compared to the estimation directly through valid-observed LST ( $R^2=0.93$ ,  $RMSE=2.02$  K,  $MAE=1.66$  K).

1) *New York City*: On the seven meteorological stations in NYC, the estimation of near-surface air temperature achieved comparable results through valid-observed LST ( $RMSE=1.42$ -



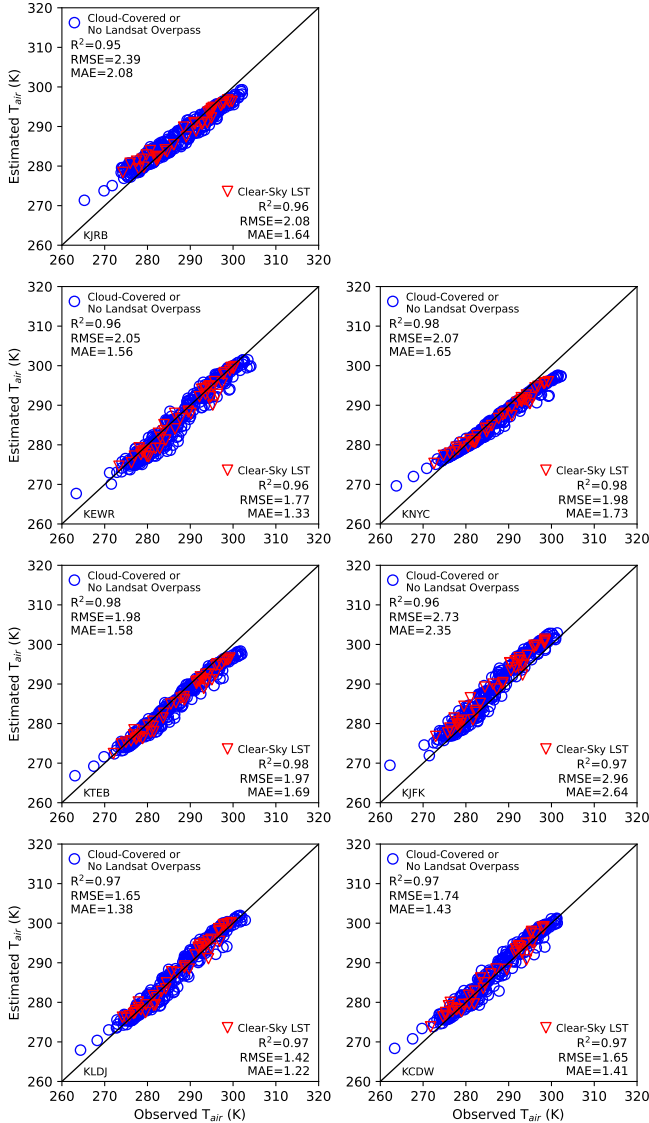


Fig. 10: Estimated near-surface air temperature via the proposed method versus in-situ near-surface air temperature from meteorological stations of New York City.

2.96 K) and reconstructed LST (RMSE=1.65-2.73 K). The performance through reconstructed LST is proportionate to the performance through valid-observed LST, meaning that reconstructed LST has consistent characteristics compared with valid-observed LST. From the scatter plots (Figure 10), we see consistency between the estimated and in-situ near-surface air temperature, except for a few data points at the lower end (below 273.15 K, or 0°C), which are likely affected by snow. We should note here that this estimation was through very simple linear regression models and by no means the optimized solution to estimate air temperature. We use this method to compare the quality of LST reconstruction only. In summary, the within 2 K estimation for air temperature demonstrates the success of LST reconstruction and its potential in generating accurate air temperature.

TABLE I: Result of estimating near-surface air temperature from the valid-observed LST situation and from reconstructed LST under cloud-covered or no Landsat overpass situations in New York City. The unit of RMSE and MAE is K.

Station	via Valid-Observed LST			via Reconstructed LST		
	R <sup>2</sup>	RMSE	MAE	R <sup>2</sup>	RMSE	MAE
KJRB	0.96	2.08	1.64	0.95	2.39	2.08
KEWR	0.96	1.77	1.33	0.96	2.05	1.56
KNYC	0.98	1.98	1.73	0.98	2.07	1.65
KTEB	0.98	1.97	1.69	0.98	1.98	1.58
KJFK	0.97	2.96	2.64	0.96	2.73	2.35
KLDJ	0.97	1.42	1.22	0.97	1.65	1.38
KCDW	0.97	1.65	1.41	0.97	1.74	1.43
NYC	0.93	2.02	1.66	0.93	2.11	1.72

TABLE II: Result of estimating near-surface air temperature from the valid-observed LST situation and from reconstructed LST under cloud-covered or no Landsat overpass situations in London. The unit of RMSE and MAE is K.

	via Valid-Observed LST			via Reconstructed LST		
	R <sup>2</sup>	RMSE	MAE	R <sup>2</sup>	RMSE	MAE
EGRB	0.99	1.64	1.38	0.98	1.43	1.18
EGWU	0.96	1.61	1.35	0.96	1.52	1.24
EGLL	0.97	1.16	1.00	0.96	1.18	0.97
EGLC	0.98	1.69	1.53	0.95	1.66	1.39
EGKB	0.95	1.37	1.20	0.97	1.06	0.85
KYL	0.98	2.05	1.70	0.96	1.89	1.58
London	0.93	1.63	1.38	0.93	1.48	1.20

2) *London*: For London, the fitting result is excellent, regardless of LST situations (Figure 11, Table II). For valid-observed situations, the fitting result combining all stations is with R<sup>2</sup> of 0.93, RMSE of 1.63 K, and MAE of 1.38 K. For each station, the range is R<sup>2</sup> of 0.95-0.99, RMSE of 1.16-2.05 K, and MAE of 1.0-1.7 K. For cloud-covered or no Landsat overpass situations, the fitting result combining all stations is R<sup>2</sup> of 0.93, RMSE of 1.63, and MAE of 1.37. For each station, the range is R<sup>2</sup> of 0.95-0.98, RMSE of 1.06-1.89, and MAE of 0.85-1.58. The performance through reconstructed LST under cloud-covered or no Landsat overpass situations is indistinguishable from the performance through valid-observed LST. In some cases the performance under cloud-cover situations is even slightly better, which can be attributed to the fact that LST under partially-cloudy and overcast conditions has better agreement with air temperature due to the blocking of direct solar radiation [46].

3) *Hong Kong*: Hong Kong has 23 valid meteorological stations; we built the linear regression models and report results on all stations in Table III, but, for demonstration purposes, only show the scatter plots of the first eight stations (alphabetically) in Figure 12. Overall, the estimation through reconstructed LST (RMSE=1.73 K) is again indistinguishable compared with the estimation through valid-observed LST (RMSE=1.71 K). The successful estimation of near-surface air temperature in all three cities demonstrates the generalization of the proposed method and indirectly validates the proposed method in LST reconstruction, especially under cloudy situations.

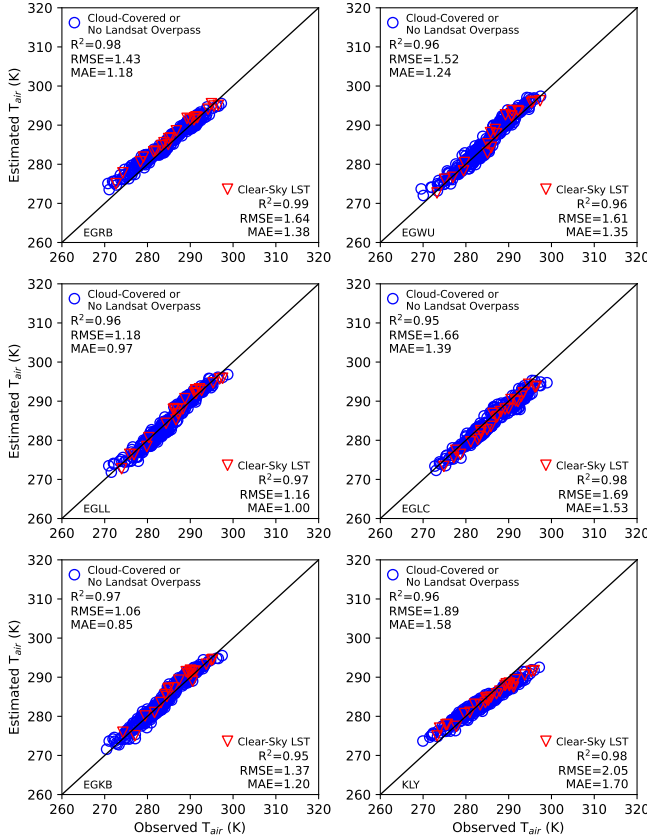


Fig. 11: Estimated near-surface air temperature via the proposed method versus in-situ near-surface air temperature from meteorological stations of London.

### E. Uncertainty Quantification

The proposed method, DELAG, is the first of its kind that can offer uncertainty quantification. To demonstrate its effectiveness, we visualize the reconstructed data, the 95% prediction intervals, and the valid-observed Landsat LST values along a vertical line ( $x$ -axis=300) in Figure 13. This particular vertical line is selected because it spans a broad range of values, from 286 K to 300 K, presenting a challenging scenario for uncertainty quantification. Within this area, DELAG achieved a RMSE of 0.568 K, with the 95% prediction intervals capturing 92.45% of the test data. Notably, the majority of the Landsat data points (red dots) fall within the 95% prediction intervals. We highlight five clusters in Figure 13 with yellow circle to demonstrate DELAG’s accuracy in estimating the 95% prediction intervals. Effective uncertainty quantification should feature dynamic confidence intervals that are neither too narrow nor too wide: overly narrow intervals suggest the model underestimates the uncertainty, while overly wide intervals indicate ineffective uncertainty quantification with little to none information. In four of the highlighted circles (1st, 2nd, 3rd, and 5th), certain regions exhibit wide 95% prediction intervals, accurately encompassing the observed data. In contrast, the 4th yellow circle and the right peak of the 2nd circle show regions with narrow 95% CI ranges that still successfully capture the observed data. This ability

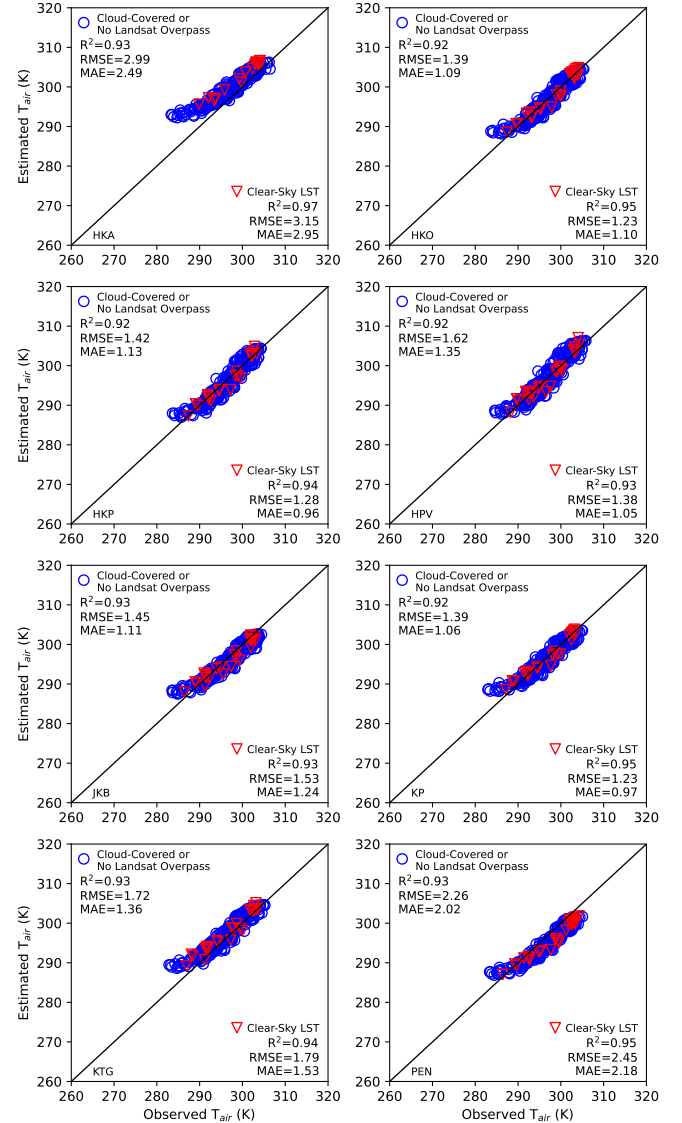


Fig. 12: Estimated near-surface air temperature via the proposed method versus in-situ near-surface air temperature from eight selected meteorological stations of Hong Kong.

to adaptively adjust the 95% prediction intervals demonstrates the proposed method’s reliability in quantifying uncertainty.

### F. Ablation Analysis

Table IV shows the comparison between the proposed method (DELAG) and baseline methods. The numbers reported here are from the first set of experiments. Compared to the baseline methods, the proposed method DELAG successfully improved the reconstruction, in terms of RMSE from 1.88 K to 0.73 K for NYC, from 3.33 K to 0.96 K for London, and from 2.50 K to 0.74 K for Hong Kong. The addition of GP greatly improved the results by minimizing bias. The addition of ensemble learning improved the model performance slightly and greatly enhanced its capability to quantify uncertainty, thus providing reliable reconstruction.

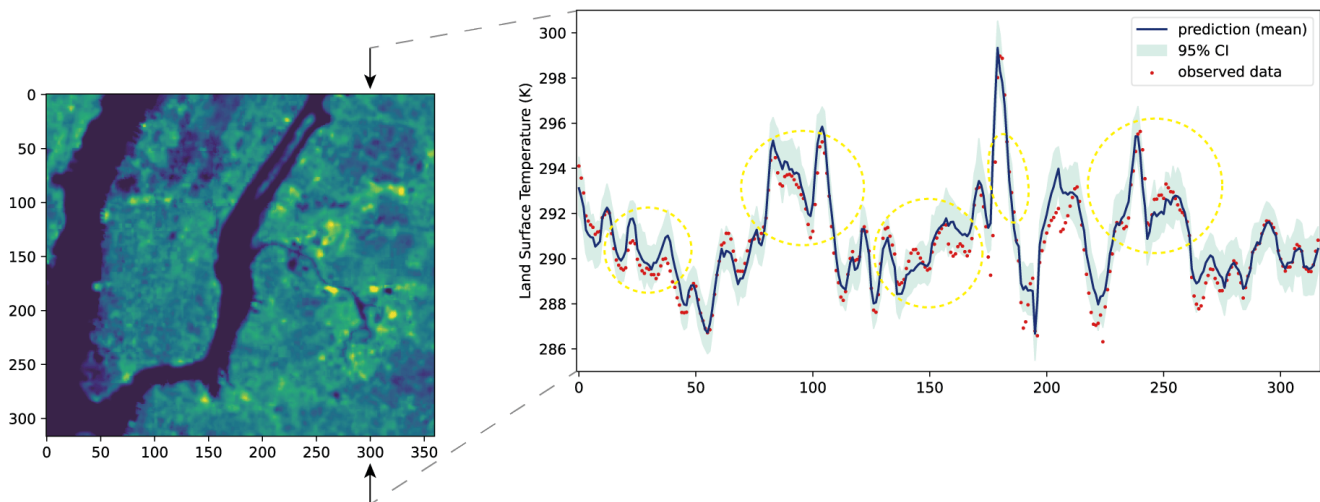


Fig. 13: Demo showing prediction mean and 95% prediction intervals along a vertical line  $[x=300]$  obtained from DELAG. Landsat observed test data are marked as red dots. Yellow circles highlighted successful uncertainty quantification in certain areas with either wide or narrow 95% prediction intervals.

TABLE III: Result of estimating near-surface air temperature from the valid-observed LST situation and from reconstructed LST under cloud-covered or no Landsat overpass situations in Hong Kong. The unit of RMSE and MAE is K.

Station	via Valid-Observed LST			via Reconstructed LST		
	$R^2$	RMSE	MAE	$R^2$	RMSE	MAE
HKA	0.97	3.15	2.95	0.93	2.99	2.49
HKO	0.95	1.23	1.10	0.92	1.39	1.09
HKP	0.94	1.28	0.96	0.92	1.42	1.13
HPV	0.93	1.38	1.05	0.92	1.62	1.35
JKB	0.93	1.53	1.24	0.93	1.45	1.11
KP	0.95	1.23	0.97	0.92	1.39	1.06
KTG	0.94	1.79	1.53	0.93	1.72	1.36
PEN	0.95	2.45	2.18	0.93	2.26	2.02
SE1	0.93	2.19	1.78	0.94	2.20	1.90
SHA	0.94	2.23	1.68	0.90	2.05	1.48
SKG	0.95	1.46	1.28	0.94	1.40	1.05
SKW	0.95	1.43	1.10	0.94	1.35	1.05
SSP	0.95	1.44	1.17	0.92	1.55	1.16
STY	0.97	0.96	0.72	0.93	1.24	0.95
TC	0.89	1.92	1.43	0.91	1.66	1.20
TMS	0.93	2.07	1.69	0.88	1.68	1.19
TU1	0.95	1.34	1.02	0.92	1.66	1.25
TWN	0.93	1.43	1.10	0.91	1.48	1.05
TY1	0.92	1.49	1.29	0.89	1.60	1.33
VP1	0.90	1.76	1.28	0.91	1.47	1.11
WLP	0.96	1.77	1.59	0.89	1.90	1.52
WTS	0.94	1.39	1.16	0.92	1.44	1.09
YLP	0.92	1.55	1.22	0.89	1.80	1.36
Hong Kong	0.91	1.71	1.34	0.89	1.73	1.32

## VI. CONCLUSION AND DISCUSSION

Having daily temperature data at high spatial resolution is critical for many applications. However, existing temperature data, such as gridMET and MODIS, cannot capture the temperature variations within cities. While Landsat is the only satellite series that provides LST data at fine scale (100 m), existing studies have overlooked its potential in generating seamless temperature data. In this study, we leverage the importance of cross-track characteristics and dual-satellite operation of Landsat since 2021 and argue that Landsat is

TABLE IV: Performance comparison between the proposed method and the baseline methods. eATC: 4-parameter enhanced ATC models; eATC<sub>e</sub>: enhanced ATC with deep ensemble learning; eATC+GP: enhanced ATC plus GP; DELAG (eATC<sub>e</sub>+GP): enhanced ATC with deep ensemble learning plus GP. The unit of RMSE, MAE and Bias is K.

	Metric	NYC	London	Hong Kong
eATC	$R^2$	0.93	0.51	0.73
	RMSE	1.88	3.33	2.50
	MAE	1.55	2.88	2.06
	Bias	1.31	2.56	1.92
	95% CI Coverage	NA	NA	NA
eATC <sub>e</sub>	$R^2$	0.96	0.84	0.83
	RMSE	1.65	2.9	2.27
	MAE	1.39	2.75	1.94
	Bias	1.31	2.56	1.92
	95% CI Coverage	60.53%	57.44%	58.86%
eATC+GP	$R^2$	0.93	0.67	0.82
	RMSE	1.55	1.86	1.29
	MAE	1.19	1.47	1.01
	Bias	0.18	0.01	0.18
	95% CI Coverage	28.88%	32.18%	31.44%
DELAG	$R^2$	0.97	0.9	0.93
	RMSE	0.73	0.96	0.74
	MAE	0.56	0.74	0.56
	Bias	-0.01	-0.27	-0.02
	95% CI Coverage	97.64%	96.41%	97.95%

a valuable source for generating seamless temperature data at high spatiotemporal resolution.

We propose DELAG, a deep ensemble learning method incorporating annual temperature cycles (ATC) and Gaussian processes (GP), for Landsat LST reconstruction. We selected three representative cities—New York City, London and Hong Kong—as study areas to show the generalization of the proposed method. We tested the proposed method under three different cloud situations. Under clear-sky situations with real-world cloud patterns, the proposed method achieved LST reconstruction with RMSE of 0.73 K, 0.96 K and 0.74 K for the three cities, respectively. Under heavily-cloudy situa-



tions, the proposed method achieved LST reconstruction with RMSE of 0.84 K, 1.62 K and 1.32 K, respectively. These results are superior to existing methods and, additionally, the proposed method can offer uncertainty quantification, providing more reliable reconstructions. We further tested the proposed method's capability to estimate near-surface air temperature using simple linear regressions. The proposed method successfully estimated near-surface air temperature with RMSE of 2.11 K, 1.48 K and 1.73 K for the three cities respectively through reconstructed LST, comparable to the estimations through valid-observed LST (RMSE of 2.02 K, 1.63 K and 1.71 K). The successful estimations of near-surface air temperature and the comparable results through reconstructed LST and valid-observed LST indirectly validate the proposed method in reconstructing seamless temperature data for real-world applications, such as examining effects of respiratory diseases and wildfire impacts [51], [24]. As existing seamless air temperature products are largely derived from satellite observations, the proposed framework and method thus provides a novel and practical pathway for real-world applications requiring seamless temperature data at high spatiotemporal resolution.

Landsat data frequency plays a major role in LST reconstruction. Landsat Next will greatly enhance data frequency, offering better data availability that is critical for daily LST reconstruction [32]. Enhancing data availability by integrating multiple LST observations can also enhance daily LST reconstruction globally. Satellites and sensors from the Sentinel satellite series, the GOES satellites, and the International Space Station can be of importance. We plan to integrate multiple satellite sources to achieve daily LST reconstruction in the future.

## REFERENCES

- [1] M. Burke, A. Driscoll, D. B. Lobell, and S. Ermon, "Using satellite imagery to understand and promote sustainable development," *Science*, vol. 371, no. 6535, p. eabe8628, 2021.
- [2] Z. Shao, Y. Liang, F. Tian, S. Song, and R. Deng, "Constructing 3-d land surface temperature model of local coal fires using uav thermal images," *IEEE Transactions on Geoscience and Remote Sensing*, vol. 60, pp. 1–9, 2022.
- [3] L. Shi, I. Kloog, A. Zanobetti, P. Liu, and J. D. Schwartz, "Impacts of temperature and its variability on mortality in new england," *Nature Climate Change*, vol. 5, no. 11, pp. 988–991, 2015.
- [4] J. G. Powers, J. B. Klemp, W. C. Skamarock, C. A. Davis, J. Dudhia, D. O. Gill, J. L. Coen, D. J. Gochis, R. Ahmadov, S. E. Peckham *et al.*, "The weather research and forecasting model: Overview, system efforts, and future directions," *Bulletin of the American Meteorological Society*, vol. 98, no. 8, pp. 1717–1737, 2017.
- [5] D. J. Weiss, P. M. Atkinson, S. Bhatt, B. Mappin, S. I. Hay, and P. W. Gething, "An effective approach for gap-filling continental scale remotely sensed time-series," *ISPRS Journal of Photogrammetry and Remote Sensing*, vol. 98, pp. 106–118, 2014.
- [6] A. F. Militino, M. D. Ugarte, U. Pérez-Goya, and M. G. Genton, "Interpolation of the mean anomalies for cloud filling in land surface temperature and normalized difference vegetation index," *IEEE Transactions on Geoscience and Remote Sensing*, vol. 57, no. 8, pp. 6068–6078, 2019.
- [7] N. K. Malakar, G. C. Hulley, S. J. Hook, K. Laraby, M. Cook, and J. R. Schott, "An operational land surface temperature product for landsat thermal data: Methodology and validation," *IEEE Transactions on Geoscience and Remote Sensing*, vol. 56, no. 10, pp. 5717–5735, 2018.
- [8] K. Li, Y. Chen, H. Xia, A. Gong, and Z. Guo, "Adjustment from temperature annual dynamics for reconstructing land surface temperature based on downscaled microwave observations," *IEEE Journal of Selected Topics in Applied Earth Observations and Remote Sensing*, vol. 13, pp. 5272–5283, 2020.
- [9] C. Zeng, D. Long, H. Shen, P. Wu, Y. Cui, and Y. Hong, "A two-step framework for reconstructing remotely sensed land surface temperatures contaminated by cloud," *ISPRS Journal of Photogrammetry and Remote Sensing*, vol. 141, pp. 30–45, 2018.
- [10] P. Wu, Z. Yin, C. Zeng, S.-B. Duan, F.-M. Göttsche, X. Ma, X. Li, H. Yang, and H. Shen, "Spatially continuous and high-resolution land surface temperature product generation: A review of reconstruction and spatiotemporal fusion techniques," *IEEE Geoscience and Remote Sensing Magazine*, vol. 9, no. 3, pp. 112–137, 2021.
- [11] Y. Xiao, W. Zhao, M. Ma, W. Yu, L. Fan, Y. Huang, X. Sun, and Q. Lang, "An integrated method for the generation of spatio-temporally continuous lst product with modis/terra observations," *IEEE Transactions on Geoscience and Remote Sensing*, vol. 61, pp. 1–14, 2023.
- [12] W. You, C. Huang, J. Hou, Y. Zhang, P. Dou, and W. Han, "Reconstruction of modis lst under cloudy conditions by integrating himawari-8 and amsr-2 data through deep forest method," *IEEE Transactions on Geoscience and Remote Sensing*, 2024.
- [13] Y. Chen, Z. Nan, Z. Cao, M. Ou, and K. Feng, "A stepwise framework for interpolating land surface temperature under cloudy conditions based on the solar-cloud-satellite geometry," *ISPRS Journal of Photogrammetry and Remote Sensing*, vol. 197, pp. 292–308, 2023.
- [14] H. Xia, Y. Chen, A. Gong, K. Li, L. Liang, and Z. Guo, "Modeling daily temperatures via a phenology-based annual temperature cycle model," *IEEE Journal of Selected Topics in Applied Earth Observations and Remote Sensing*, vol. 14, pp. 6219–6229, 2021.
- [15] J. Quan, Y. Guan, W. Zhan, T. Ma, D. Wang, and Z. Guo, "Generating 60–100 m, hourly, all-weather land surface temperatures based on the landsat, ecostress, and reanalysis temperature combination (lerc)," *ISPRS Journal of Photogrammetry and Remote Sensing*, vol. 205, pp. 115–134, 2023.
- [16] A. R. Stine, P. Huybers, and I. Y. Fung, "Changes in the phase of the annual cycle of surface temperature," *Nature*, vol. 457, no. 7228, pp. 435–440, 2009.
- [17] F. Hong, W. Zhan, F.-M. Göttsche, J. Lai, Z. Liu, L. Hu, P. Fu, F. Huang, J. Li, H. Li *et al.*, "A simple yet robust framework to estimate accurate daily mean land surface temperature from thermal observations of tandem polar orbiters," *Remote Sensing of Environment*, vol. 264, p. 112612, 2021.
- [18] Y. Yang, W. Zhao, Y. Yang, M. Xu, H. Mukhtar, G. Tauqir, and P. Tarolli, "An annual temperature cycle feature constrained method for generating modis daytime all-weather land surface temperature," *IEEE Transactions on Geoscience and Remote Sensing*, 2024.
- [19] P. Fu and Q. Weng, "Consistent land surface temperature data generation from irregularly spaced landsat imagery," *Remote Sensing of Environment*, vol. 184, pp. 175–187, 2016.
- [20] Y. Chen, J. Wu, K. Yu, and D. Wang, "Evaluating the impact of the building density and height on the block surface temperature," *Building and Environment*, vol. 168, p. 106493, 2020.
- [21] V. C. Broto and H. Bulkeley, "A survey of urban climate change experiments in 100 cities," *Global Environmental Change*, vol. 23, no. 1, pp. 92–102, 2013.
- [22] A. Gasparri, P. Masselot, M. Scortichini, R. Schneider, M. N. Mistry, F. Sera, H. L. Macintyre, R. Phalkey, and A. M. Vicedo-Cabrera, "Small-area assessment of temperature-related mortality risks in england and wales: a case time series analysis," *The Lancet Planetary Health*, vol. 6, no. 7, pp. e557–e564, 2022.
- [23] C. Luo, J. Qian, Y. Liu, Q. Lv, Y. Ma, and F. Yin, "Long-term air pollution levels modify the relationships between short-term exposure to meteorological factors, air pollution and the incidence of hand, foot and mouth disease in children: a dlmm-based multicity time series study in sichuan province, china," *BMC Public Health*, vol. 22, no. 1, p. 1484, 2022.
- [24] S. Liu and H. C. Ho, "Effects of socioeconomic status and greenspace on respiratory emergency department visits under short-term temperature variations: An age-stratified case time-series study," *Social Science & Medicine*, vol. 343, p. 116613, 2024.
- [25] M. D. Yazdi, Y. Wang, Q. Di, W. J. Requia, Y. Wei, L. Shi, M. B. Sabath, F. Dominici, B. Coull, J. S. Evans *et al.*, "Long-term effect of exposure to lower concentrations of air pollution on mortality among us medicare participants and vulnerable subgroups: a doubly-robust approach," *The Lancet Planetary Health*, vol. 5, no. 10, pp. e689–e697, 2021.

- [26] K. Dahl, R. Licker, J. T. Abatzoglou, and J. Decler-Barreto, "Increased frequency of and population exposure to extreme heat index days in the united states during the 21st century," *Environmental Research Communications*, vol. 1, no. 7, p. 075002, 2019.
- [27] A. Jiao, Y. Sun, C. Avila, V. Chiu, J. Slezak, D. A. Sacks, J. T. Abatzoglou, J. Molitor, J.-C. Chen, T. Benmarhnia *et al.*, "Analysis of heat exposure during pregnancy and severe maternal morbidity," *JAMA Network Open*, vol. 6, no. 9, pp. e2332780–e2332780, 2023.
- [28] X. Zhu, S.-B. Duan, Z.-L. Li, P. Wu, H. Wu, W. Zhao, and Y. Qian, "Reconstruction of land surface temperature under cloudy conditions from landsat 8 data using annual temperature cycle model," *Remote Sensing of Environment*, vol. 281, p. 113261, 2022.
- [29] I. Kloog, S. J. Melly, B. A. Coull, F. Nordio, and J. D. Schwartz, "Using satellite-based spatiotemporal resolved air temperature exposure to study the association between ambient air temperature and birth outcomes in massachusetts," *Environmental Health Perspectives*, vol. 123, no. 10, pp. 1053–1058, 2015.
- [30] J. Hooker, G. Duveiller, and A. Cescatti, "A global dataset of air temperature derived from satellite remote sensing and weather stations," *Scientific data*, vol. 5, no. 1, pp. 1–11, 2018.
- [31] W. Zhao and S.-B. Duan, "Reconstruction of daytime land surface temperatures under cloud-covered conditions using integrated modis/terra land products and msg geostationary satellite data," *Remote Sensing of Environment*, vol. 247, p. 111931, 2020.
- [32] J. R. Irons, J. L. Dwyer, and J. A. Barsi, "The next landsat satellite: The landsat data continuity mission," *Remote Sensing of Environment*, vol. 122, pp. 11–21, 2012.
- [33] V. Kovalsky and D. P. Roy, "The global availability of landsat 5 tm and landsat 7 etm+ land surface observations and implications for global 30 m landsat data product generation," *Remote Sensing of Environment*, vol. 130, pp. 280–293, 2013.
- [34] R. Heffernan, F. Mostashari, D. Das, A. Karpati, M. Kulldorff, D. Weiss *et al.*, "Syndromic surveillance in public health practice, new york city," *Emerg Infect Dis*, vol. 10, no. 5, pp. 858–864, 2004.
- [35] S. K. Greene, S. F. McGough, G. M. Culp, L. E. Graf, M. Lipsitch, N. A. Menzies, and R. Kahn, "Nowcasting for real-time covid-19 tracking in new york city: an evaluation using reportable disease data from early in the pandemic," *JMIR Public Health and Surveillance*, vol. 7, no. 1, p. e25538, 2021.
- [36] P. Murage, S. Kovats, C. Sarran, J. Taylor, R. McInnes, and S. Hajat, "What individual and neighbourhood-level factors increase the risk of heat-related mortality? a case-crossover study of over 185,000 deaths in london using high-resolution climate datasets," *Environment International*, vol. 134, p. 105292, 2020.
- [37] M. Abed Al Ahad, U. Demšar, F. Sullivan, and H. Kulu, "The spatial-temporal effect of air pollution on individuals' reported health and its variation by ethnic groups in the united kingdom: a multilevel longitudinal analysis," *BMC Public Health*, vol. 23, no. 1, p. 897, 2023.
- [38] H. Hersbach, B. Bell, P. Berrisford, S. Hirahara, A. Horányi, J. Muñoz-Sabater, J. Nicolas, C. Peubey, R. Radu, D. Schepers *et al.*, "The era5 global reanalysis," *Quarterly Journal of the Royal Meteorological Society*, vol. 146, no. 730, pp. 1999–2049, 2020.
- [39] J. Gardner, G. Pleiss, K. Q. Weinberger, D. Bindel, and A. G. Wilson, "Gpytorch: Blackbox matrix-matrix gaussian process inference with gpu acceleration," *Advances in Neural Information Processing Systems*, vol. 31, 2018.
- [40] D. P. Kingma, "Adam: A method for stochastic optimization," *arXiv preprint arXiv:1412.6980*, 2014.
- [41] G. Huang, Y. Li, G. Pleiss, Z. Liu, J. E. Hopcroft, and K. Q. Weinberger, "Snapshot ensembles: Train 1, get m for free," *arXiv preprint arXiv:1704.00109*, 2017.
- [42] P. Izmailov, D. Podoprikin, T. Garipov, D. Vetrov, and A. G. Wilson, "Averaging weights leads to wider optima and better generalization," *arXiv preprint arXiv:1803.05407*, 2018.
- [43] T. Garipov, P. Izmailov, D. Podoprikin, D. P. Vetrov, and A. G. Wilson, "Loss surfaces, mode connectivity, and fast ensembling of dnns," *Advances in Neural Information Processing Systems*, vol. 31, 2018.
- [44] T. Gneiting and A. E. Raftery, "Weather forecasting with ensemble methods," *Science*, vol. 310, no. 5746, pp. 248–249, 2005.
- [45] S.-J. Liu, H. Luo, and Q. Shi, "Active ensemble deep learning for polarimetric synthetic aperture radar image classification," *IEEE Geoscience and Remote Sensing Letters*, vol. 18, no. 9, pp. 1580–1584, 2020.
- [46] C. Vancutsem, P. Ceccato, T. Dinku, and S. J. Connor, "Evaluation of modis land surface temperature data to estimate air temperature in different ecosystems over africa," *Remote Sensing of Environment*, vol. 114, no. 2, pp. 449–465, 2010.
- [47] J. L. White-Newsome, S. J. Brines, D. G. Brown, J. T. Dvonch, C. J. Gronlund, K. Zhang, E. M. Oswald, and M. S. O'Neill, "Validating satellite-derived land surface temperature with in situ measurements: A public health perspective," *Environmental health perspectives*, vol. 121, no. 8, pp. 925–931, 2013.
- [48] N. Janatian, M. Sadeghi, S. H. Sanaeinejad, E. Bakhshian, A. Farid, S. M. Hasheminia, and S. Ghazanfari, "A statistical framework for estimating air temperature using modis land surface temperature data," *International Journal of Climatology*, vol. 37, no. 3, pp. 1181–1194, 2017. [Online]. Available: <https://rmets.onlinelibrary.wiley.com/doi/abs/10.1002/joc.4766>
- [49] A. Paszke, S. Gross, F. Massa, A. Lerer, J. Bradbury, G. Chanan, T. Killeen, Z. Lin, N. Gimelshein, L. Antiga *et al.*, "Pytorch: An imperative style, high-performance deep learning library," *Advances in neural information processing systems*, vol. 32, 2019.
- [50] R. E. Dickinson, "Land surface processes and climate—surface albedos and energy balance," in *Advances in Geophysics*. Elsevier, 1983, vol. 25, pp. 305–353.
- [51] G. Chen, Y. Guo, X. Yue, S. Tong, A. Gasparri, M. L. Bell, B. Armstrong, J. Schwartz, J. J. Jaakkola, A. Zanobetti *et al.*, "Mortality risk attributable to wildfire-related pm<sub>2.5</sub> pollution: a global time series study in 749 locations," *The Lancet Planetary Health*, vol. 5, no. 9, pp. e579–e587, 2021.